Impact of intraocular pressure on changes of blood flow in the retina, choroid, and optic nerve head in rats investigated by optical microangiography

Zhongwei Zhi,[1] William O. Cepurna,[2] Elaine C. Johnson,[2] John C. Morrison,[2] and Ruikang K. Wang[1,3,*]

[1]*Department of Bioengineering, University of Washington, Seattle, WA 98195, USA*
[2]*Dept. of Ophthalmology, Casey Eye Institute, Oregon Health & Science University, Portland, OR 97239, USA*
[3]*Department of Ophthalmology, University of Washington, Seattle, WA 98195, USA*
*wangrk@uw.edu

Abstract: In this paper, we demonstrate the use of optical coherence tomography/optical microangiography (OCT/OMAG) to image and measure the effects of acute intraocular pressure (IOP) elevation on retinal, choroidal and optic nerve head (ONH) perfusion in the rat eye. In the experiments, IOP was elevated from 10 to 100 mmHg in 10 mmHg increments. At each IOP level, three-dimensional data volumes were captured using an ultrahigh sensitive (UHS) OMAG scanning protocol for 3D volumetric perfusion imaging, followed by repeated B-scans for Doppler OMAG analysis to determine blood flow velocity. Velocity and vessel diameter measurements were used to calculate blood flow in selected retinal blood vessels. Choroidal perfusion was calculated by determining the peripapillary choroidal filling at each pressure level and calculating this as a percentage of area filling at baseline (10 mmHg). ONH blood perfusion was calculated as the percentage of blood flow area over a segmented ONH area to a depth 150 microns posterior to the choroidal opening. We show that volumetric blood flow reconstructions revealed detailed 3D maps, to the capillary level, of the retinal, choroidal and ONH microvasculature, revealing retinal arterioles, capillaries and veins, the choroidal opening and a consistent presence of the central retinal artery inferior to the ONH. While OCT structural images revealed a reversible compression of the ONH and vasculature with elevated IOP, OMAG successfully documented changes in retinal, choroidal and ONH blood perfusion and allowed quantitative measurements of these changes. Starting from 30 mm Hg, retinal blood flow (RBF) diminished linearly with increasing IOP and was nearly extinguished at 100 mm Hg, with full recovery after return of IOP to baseline. Choroidal filling was unaffected until IOP reached 60 mmHg, then decreased to 20% of baseline at IOP 100 mmHg, and normalized when IOP returned to baseline. A reduction in ONH blood perfusion at higher IOP's was also observed, but shadow from overlying retinal vessels at lower IOP's limited precise measurements of changes in ONH capillary perfusion compared to baseline. Therefore, OCT/OMAG can be a useful tool to image and measure blood flow in the retina, choroidal and ONH of the rat eye as well as document the effects of elevated IOP on blood flow in these vascular beds.

References and links

1. J. Flammer, S. Orgül, V. P. Costa, N. Orzalesi, G. K. Krieglstein, L. M. Serra, J. P. Renard, and E. Stefánsson, "The impact of ocular blood flow in glaucoma," Prog. Retin. Eye Res. **21**(4), 359–393 (2002).
2. M. C. Grieshaber and J. Flammer, "Blood flow in glaucoma," Curr. Opin. Ophthalmol. **16**(2), 79–83 (2005).
3. J. E. Grunwald, J. Piltz, S. M. Hariprasad, and J. DuPont, "Optic nerve and choroidal circulation in glaucoma," Invest. Ophthalmol. Vis. Sci. **39**(12), 2329–2336 (1998).
4. C. E. Riva, J. E. Grunwald, and B. L. Petrig, "Autoregulation of human retinal blood flow. An investigation with laser Doppler velocimetry," Invest. Ophthalmol. Vis. Sci. **27**(12), 1706–1712 (1986).
5. K. R. Brein and C. E. Riva, "Laser Doppler velocimetry measurement of pulsatile blood flow in capillary tubes," Microvasc. Res. **24**(1), 114–118 (1982).
6. C. E. Riva, J. E. Grunwald, S. H. Sinclair, and B. L. Petrig, "Blood velocity and volumetric flow rate in human retinal vessels," Invest. Ophthalmol. Vis. Sci. **26**(8), 1124–1132 (1985).
7. F. Binaghi, F. Cannas, and F. Pitzus, "La flussimetria Doppler laser. Principi ed applicazioni cliniche nelle acrosindromi vascolari [Laser Doppler flowmetry. principles and clinical applications in vascular acro-syndromes]," Minerva Med. **79**(10), 831–838 (1988).
8. C. E. Riva, "Basic principles of laser Doppler flowmetry and application to the ocular circulation," Int. Ophthalmol. **23**(4/6), 183–189 (2001).
9. Z. He, C. T. Nguyen, J. A. Armitage, A. J. Vingrys, and B. V. Bui, "Blood pressure modifies retinal susceptibility to intraocular pressure elevation," PLoS ONE **7**(2), e31104 (2012).
10. A. Harris, D. R. Anderson, L. Pillunat, K. Joos, R. W. Knighton, L. Kagemann, and B. J. Martin, "Laser Doppler flowmetry measurement of changes in human optic nerve head blood flow in response to blood gas perturbations," J. Glaucoma **5**(4), 258–265 (1996).
11. C. E. Riva, S. Harino, B. L. Petrig, and R. D. Shonat, "Laser Doppler flowmetry in the optic nerve," Exp. Eye Res. **55**(3), 499–506 (1992).
12. K. Yaoeda, M. Shirakashi, S. Funaki, H. Funaki, T. Nakatsue, and H. Abe, "Measurement of microcirculation in the optic nerve head by laser speckle flowgraphy and scanning laser Doppler flowmetry," Am. J. Ophthalmol. **129**(6), 734–739 (2000).
13. B. L. Petrig, C. E. Riva, and S. S. Hayreh, "Laser Doppler flowmetry and optic nerve head blood flow," Am. J. Ophthalmol. **127**(4), 413–425 (1999).
14. D. Huang, E. A. Swanson, C. P. Lin, J. S. Schuman, W. G. Stinson, W. Chang, M. R. Hee, T. Flotte, K. Gregory, C. A. Puliafito, and J. G. Fujimoto, "Optical coherence tomography," Science **254**(5035), 1178–1181 (1991).
15. D. S. Chauhan and J. Marshall, "The interpretation of optical coherence tomography images of the retina," Invest. Ophthalmol. Vis. Sci. **40**(10), 2332–2342 (1999).
16. M. E. van Velthoven, D. J. Faber, F. D. Verbraak, T. G. van Leeuwen, and M. D. de Smet, "Recent developments in optical coherence tomography for imaging the retina," Prog. Retin. Eye Res. **26**(1), 57–77 (2007).
17. R. Leitgeb, L. Schmetterer, W. Drexler, A. Fercher, R. Zawadzki, and T. Bajraszewski, "Real-time assessment of retinal blood flow with ultrafast acquisition by color Doppler Fourier domain optical coherence tomography," Opt. Express **11**(23), 3116–3121 (2003).
18. B. White, M. Pierce, N. Nassif, B. Cense, B. Park, G. Tearney, B. Bouma, T. Chen, and J. de Boer, "In vivo dynamic human retinal blood flow imaging using ultra-high-speed spectral domain optical coherence tomography," Opt. Express **11**(25), 3490–3497 (2003).
19. Y. Wang, A. A. Fawzi, R. Varma, A. A. Sadun, X. Zhang, O. Tan, J. A. Izatt, and D. Huang, "Pilot study of optical coherence tomography measurement of retinal blood flow in retinal and optic nerve diseases," Invest. Ophthalmol. Vis. Sci. **52**(2), 840–845 (2011).
20. R. K. Wang, S. L. Jacques, Z. Ma, S. Hurst, S. R. Hanson, and A. Gruber, "Three dimensional optical angiography," Opt. Express **15**(7), 4083–4097 (2007).
21. Y. Zhao, Z. Chen, C. Saxer, S. Xiang, J. F. de Boer, and J. S. Nelson, "Phase-resolved optical coherence tomography and optical Doppler tomography for imaging blood flow in human skin with fast scanning speed and high velocity sensitivity," Opt. Lett. **25**(2), 114–116 (2000).
22. R. K. Wang and L. An, "Doppler optical micro-angiography for volumetric imaging of vascular perfusion in vivo," Opt. Express **17**(11), 8926–8940 (2009).
23. L. An, J. Qin, and R. K. Wang, "Ultrahigh sensitive optical microangiography for in vivo imaging of microcirculations within human skin tissue beds," Opt. Express **18**(8), 8220–8228 (2010).
24. R. K. Wang, L. An, P. Francis, and D. J. Wilson, "Depth-resolved imaging of capillary networks in retina and choroid using ultrahigh sensitive optical microangiography," Opt. Lett. **35**(9), 1467–1469 (2010).
25. Z. Zhi, W. Cepurna, E. Johnson, T. Shen, J. Morrison, and R. K. Wang, "Volumetric and quantitative imaging of retinal blood flow in rats with optical microangiography," Biomed. Opt. Express **2**(3), 579–591 (2011).
26. R. Varma, P. P. Lee, I. Goldberg, and S. Kotak, "An assessment of the health and economic burdens of glaucoma," Am. J. Ophthalmol. **152**(4), 515–522 (2011).
27. M. D. Roberts, I. A. Sigal, Y. Liang, C. F. Burgoyne, and J. C. Downs, "Changes in the biomechanical response of the optic nerve head in early experimental glaucoma," Invest. Ophthalmol. Vis. Sci. **51**(11), 5675–5684 (2010).
28. J. C. Morrison, W. O. Cepurna, Y. Guo, and E. C. Johnson, "Pathophysiology of human glaucomatous optic nerve damage: insights from rodent models of glaucoma," Exp. Eye Res. **93**(2), 156–164 (2011).
29. I. H. Pang and A. F. Clark, "Rodent models for glaucoma retinopathy and optic neuropathy," J. Glaucoma **16**(5), 483–505 (2007).

30. Y. Guo, E. C. Johnson, W. O. Cepurna, J. A. Dyck, T. Doser, and J. C. Morrison, "Early gene expression changes in the retinal ganglion cell layer of a rat glaucoma model," Invest. Ophthalmol. Vis. Sci. **52**(3), 1460–1473 (2011).
31. E. C. Johnson, T. A. Doser, W. O. Cepurna, J. A. Dyck, L. Jia, Y. Guo, W. S. Lambert, and J. C. Morrison, "Cell proliferation and interleukin-6-type cytokine signaling are implicated by gene expression responses in early optic nerve head injury in rat glaucoma," Invest. Ophthalmol. Vis. Sci. **52**(1), 504–518 (2011).
32. Y. Liang, J. C. Downs, B. Fortune, G. Cull, G. A. Cioffi, and L. Wang, "Impact of systemic blood pressure on the relationship between intraocular pressure and blood flow in the optic nerve head of nonhuman primates," Invest. Ophthalmol. Vis. Sci. **50**(5), 2154–2160 (2009).
33. Z. Zhi, Y. Jung, Y. Jia, L. An, and R. K. Wang, "Highly sensitive imaging of renal microcirculation in vivo using ultrahigh sensitive optical microangiography," Biomed. Opt. Express **2**(5), 1059–1068 (2011).
34. T. Fukuchi, K. Takahashi, and K. Shou, "Optical coherence tomography (OCT) findings in normal retina and laser-induced choroidal neovascularization in rats," Graefes Arch. Clin. Exp. Ophthalmol. **239**(1), 41–46 (2001).
35. V. J. Srinivasan, J. Y. Jiang, M. A. Yaseen, H. Radhakrishnan, W. Wu, S. Barry, A. E. Cable, and D. A. Boas, "Rapid volumetric angiography of cortical microvasculature with optical coherence tomography," Opt. Lett. **35**(1), 43–45 (2010).
36. C. Geijer and A. Bill, "Effects of raised intraocular pressure on retinal, prelaminar, laminar, and retrolaminar optic nerve blood flow in monkeys," Invest. Ophthalmol. Vis. Sci. **18**(10), 1030–1042 (1979).
37. Z. He, A. J. Vingrys, J. A. Armitage, and B. V. Bui, "The role of blood pressure in glaucoma," Clin. Exp. Optom. **94**(2), 133–149 (2011).
38. Y. Jia, P. Li, and R. K. Wang, "Optical microangiography provides an ability to monitor responses of cerebral microcirculation to hypoxia and hyperoxia in mice," J. Biomed. Opt. **16**(9), 096019 (2011).
39. Y. Jia, P. Li, S. Dziennis, and R. K. Wang, "Responses of peripheral blood flow to acute hypoxia and hyperoxia as measured by optical microangiography," PLoS ONE **6**(10), e26802 (2011).
40. J. C. Morrison, E. Johnson, and W. O. Cepurna, "Rat models for glaucoma research," Prog. Brain Res. **173**, 285–301 (2008).
41. B. Fortune, T. E. Choe, J. Reynaud, C. Hardin, G. A. Cull, C. F. Burgoyne, and L. Wang, "Deformation of the rodent optic nerve head and peripapillary structures during acute intraocular pressure elevation," Invest. Ophthalmol. Vis. Sci. **52**(9), 6651–6661 (2011).
42. J. C. Morrison, C. G. Moore, L. M. Deppmeier, B. G. Gold, C. K. Meshul, and E. C. Johnson, "A rat model of chronic pressure-induced optic nerve damage," Exp. Eye Res. **64**(1), 85–96 (1997).
43. J. C. Morrison, E. C. Johnson, W. O. Cepurna, and R. H. Funk, "Microvasculature of the rat optic nerve head," Invest. Ophthalmol. Vis. Sci. **40**(8), 1702–1709 (1999).
44. C. Dai, P. T. Khaw, Z. Q. Yin, D. Li, G. Raisman, and Y. Li, "Structural basis of glaucoma: the fortified astrocytes of the optic nerve head are the target of raised intraocular pressure," Glia **60**(1), 13–28 (2012).
45. M. Pazos, S. Gardiner, J. G. J. Reynaud, W. O. Cepurna, E. C. Johnson, J. C. Morrison, C. F. Burgoyne, and H. Yang, "Radial optic nerve expansion within the expanding scleral canal in the hypertonic saline rat early experimental glaucoma (EEG) model," Invest. Ophthalmol. Vis. Sci. **51**, 4806 (2010).
46. B. V. Bui, B. Edmunds, G. A. Cioffi, and B. Fortune, "The gradient of retinal functional changes during acute intraocular pressure elevation," Invest. Ophthalmol. Vis. Sci. **46**(1), 202–213 (2005).
47. L. Fizanne, B. Fromy, M. P. Preckel, D. Sigaudo-Roussel, and J. L. Saumet, "Effect of isoflurane on skin-pressure-induced vasodilation," J. Vasc. Res. **40**(4), 416–422 (2003).
48. R. F. Leoni, F. F. Paiva, E. C. Henning, G. C. Nascimento, A. Tannús, D. B. de Araujo, and A. C. Silva, "Magnetic resonance imaging quantification of regional cerebral blood flow and cerebrovascular reactivity to carbon dioxide in normotensive and hypertensive rats," Neuroimage **58**(1), 75–81 (2011).
49. W. C. Seyde and D. E. Longnecker, "Cerebral oxygen tension in rats during deliberate hypotension with sodium nitroprusside, 2-chloroadenosine, or deep isoflurane anesthesia," Anesthesiology **64**(4), 480–485 (1986).
50. G. Weigert, O. Findl, A. Luksch, G. Rainer, B. Kiss, C. Vass, and L. Schmetterer, "Effects of moderate changes in intraocular pressure on ocular hemodynamics in patients with primary open-angle glaucoma and healthy controls," Ophthalmology **112**(8), 1337–1342 (2005).
51. L. E. Pillunat, D. R. Anderson, R. W. Knighton, K. M. Joos, and W. J. Feuer, "Autoregulation of human optic nerve head circulation in response to increased intraocular pressure," Exp. Eye Res. **64**(5), 737–744 (1997).
52. C. E. Riva, S. D. Cranstoun, and B. L. Petrig, "Effect of decreased ocular perfusion pressure on blood flow and the flicker-induced flow response in the cat optic nerve head," Microvasc. Res. **52**(3), 258–269 (1996).
53. N. Sossi and D. R. Anderson, "Effect of elevated intraocular pressure on blood flow. Occurrence in cat optic nerve head studied with iodoantipyrine I 125," Arch. Ophthalmol. **101**(1), 98–101 (1983).
54. A. Alm and A. Bill, "The oxygen supply to the retina. II. Effects of high intraocular pressure and of increased arterial carbon dioxide tension on uveal and retinal blood flow in cats. A study with radioactively labelled microspheres including flow determinations in brain and some other tissues," Acta Physiol. Scand. **84**(3), 306–319 (1972).
55. J. W. Kiel and A. P. Shepherd, "Autoregulation of choroidal blood flow in the rabbit," Invest. Ophthalmol. Vis. Sci. **33**(8), 2399–2410 (1992).
56. E. Polska, C. Simader, G. Weigert, A. Doelemeyer, J. Kolodjaschna, O. Scharmann, and L. Schmetterer, "Regulation of choroidal blood flow during combined changes in intraocular pressure and arterial blood pressure," Invest. Ophthalmol. Vis. Sci. **48**(8), 3768–3774 (2007).

1. Introduction

Perfusion of the retina, choroid and optic nerve head (ONH) is critical to maintaining normal vision, and reduction in perfusion may contribute to the development and progression of various ocular diseases, including glaucoma [1–3]. The development of non-invasive methods for assessing blood flow in these structures is therefore important for both patient care and research.

Many different methods have been used to visualize and measure directly or calculate indirectly in vivo ocular blood flow (OBF). Laser Doppler velocimetry (LDV) [4–6] is used to measure RBF velocity by using a laser beam directed at a specific blood vessel, and the Doppler shift caused by moving red blood cells allows blood speed to be measured. However, this method only provides information on flow in a single vessel, but no information about perfusion in the rest of the eye. Unlike velocimetry, laser Doppler flowmetry (LDF) [7–9] can measure relative velocities, numbers of red blood cells and flux at a fixed spot, particularly in capillary beds with the laser directed to areas between larger vessels, and it has often been used for blood flow measurement in the optic nerve [10–13]. One main drawback of LDF is that measurements are limited to a small selected area and the exact volume of the tissue being measured is unknown, which restricts the reproducibility of measurements with this technique.1 Optical coherence tomography (OCT) [14] is a non-contact, non-invasive imaging modality that has been widely used for human eye imaging [15,16] and, when combined with the Doppler principle, can be used to measure retinal blood flow [17–19]. As a variation of Spectral-domain optical coherence tomography (SDOCT), Optical microangiography (OMAG) [20] is capable of generating 3D dynamic perfusion images of tissue microcirculation. When combined with phase-resolved analysis methods developed for Doppler OCT [21], it produces Doppler OMAG (D-OMAG) [22] that can be used for quantitative and directional blood flow imaging, with improved low-flow detection as compared to phase-resolved Doppler OCT. Recently, it has been refined into ultra-high sensitive OMAG (UHS-OMAG) [23,24] which has the capability of imaging capillary vessels with speed as slow as 4 µm/s. The combined use of D-OMAG and UHS-OMAG to provide simultaneous 3D angiography and quantitative measurement of blood flow in rat retinal blood vessels has recently been described [25].

Glaucoma is currently estimated to affect nearly 3% of the world's adult population, with a significant economic and individual impact [26]. Despite its prominent contribution to worldwide blindness, mechanisms of optic nerve damage in this condition are incompletely understood, although recent refinements in existing models of primate glaucoma [27] and development of several experimental and spontaneous glaucoma models in rodents [28,29] are improving our knowledge of the retinal and optic nerve head responses to elevated intraocular pressure (IOP) [30,31]. Because elevating IOP is also known to affect retinal and ONH perfusion [25,32], visualizing and measuring these blood flow effects become increasingly important, if we are to fully understand the range of mechanisms that may be contributing to nerve damage in glaucoma.

The purpose of this study is to demonstrate the ability of OCT/OMAG to image the tissue and vascular anatomy of the rat retina, ONH and surrounding choroid and investigate the effects of acutely elevated IOP on this anatomy. In addition, we will present quantitative measurements of the effect of elevated IOP on these important vascular beds, as determined by this technique.

2. Material and methods

2.1. Animal model

All animals were treated in accordance with the ARVO Statement for the Use of Animals in Ophthalmic and Vision Research. Adult Brown Norway rats (N = 6), anesthetized with inhalational isoflurane (1.5%) mixed with 80% air and 20% oxygen, were positioned for OCT/OMAG imaging in custom-made head holders. IOP was elevated by cannulation of the anterior chamber with a 5 millimeter long 31 gauge needle connected to a reservoir filled with

balanced salt solution and to a calibrated pressure transducer. The height of the reservoir was used to elevate IOP, as determined by the transducer, in 10 mm Hg increments, from 10 mm Hg (treated as baseline) to 80 mmHg followed by a pressure of 100 mmHg, which produced complete obstruction of ocular blood flow. After that, IOP was reduced back to 10 mmHg to examine reperfusion. In separate experiments, double-cannulated closed artificial chambers and anterior chambers of anesthetized animals were connected with one cannula (via a 23 gauge needle) to a pressure transducer and the other (via a 31 gauge needle) to a suspended reservoir and second transducer, as described above. Over a range of reservoir heights and pressures, both transducers demonstrated excellent agreement (data not shown), following several seconds for equilibration. During the whole process, animal position was unchanged and there was no apparent eye movement. After the in vivo imaging session, each animal was euthanized.

2.2. Optical coherence tomography/optical microangiography system

OMAG, as an extension of SDOCT, shares the same system setup with SDOCT. The OMAG system we applied here has been described in detail [25]. Here we will briefly provide parameters that specifically determine the system performance for imaging the rat eye. The system was operated at a wavelength of 1300 nm, in contrast to conventional OCT systems that normally use 800 nm wavelength light source for imaging. Since the water absorption over the short length of the rodent eye is not significant enough to reduce the system sensitivity, we demonstrate that 1300 nm, in addition to an 800 nm light source, can be used for the rodent retinal imaging, opening up new choice of light source. The axial resolution is 12 μm and the lateral resolution is ~16 μm in air. The maximal imaging speed of the system was 92,000 A scans per second, which is nearly doubled compared to the one we applied previously [25]. At this A scan rate, the measured signal to noise ratio (SNR) was ~100 dB at the focus spot of the sampling beam, which was ~500 μm below the zero delay line. The total depth range was measured to be ~2.8 mm in air (which is equivalent to 2.1 mm in biological tissue, assuming a sample refractive index of ~1.35) and the power incidence on the sample was measured to be ~1mW.

2.3. Image acquisition and processing

For all image acquisition, the pupil was dilated with 1% tropicamide and 2.5% phenylephrine eyedrops, and the position of the rat eye was kept stationary using a custom-made animal holder during the entire process of IOP elevation. At each IOP level, 3D data volumes covering the ONH area with a size of ~1x1 mm^2 were first captured using the UHS-OMAG scanning protocol [33], in which the raster scanning of the beam spot was performed to capture 256 A-lines within each B-frame (2D cross-sectional image) and 1000 B-frames for each C-scan (3D image). Using a frame rate of 280 frames per second (fps), we were able to obtain a single 3D data volume in only 3 seconds, which helps minimize motion artifact. We then applied repeated B-scans (using 3000 A-lines per B-frame and a frame rate of 10 fps) at one cross-section for D-OMAG analysis [22,34] to determine the axial blood flow velocity in selected retinal arteries/veins. This switch between UHS-OMAG and D-OMAG imaging protocols was automatically controlled by the controlling software written in Labview. At each IOP level, after the height of the reservoir was increased, we waited about 1 minute before OCT scans were taken to ensure that the IOP would be stable when the OCT scans were taken.

3D blood flow images were reconstructed from the 3D data volumes by applying high pass filtering along the slow scan direction to separate the moving blood flow from static tissues. Since we shifted the high pass filtering process from the fast scan direction to the slow scan direction [35], the time interval available for Doppler analysis was increased from 0.01 ms (between adjacent A-lines) to 3.57 ms (between adjacent B-frames), which dramatically improved the sensitivity of the system to slow flow movements, enabling us to image capillary flow within the retina and ONH.

2.4. RBF, choroidal and ONH blood flow calculation

The method we used for RBF calculation has been described in detail [25]. We selected specific retinal arteries/veins for blood flow calculation, using vessel branches located near the ONH. The axial velocity of each vessel was determined from a D-OMAG cross-sectional phase image by calculating the phase difference between adjacent A-lines. The axial velocity VZ can be given as

$$V_Z = \frac{\Delta\varphi \cdot \lambda_0}{4\pi n \Delta t_A} \qquad (1)$$

where λ_0 is the central wavelength, n is the refractive index, $\Delta\varphi$ is the phase difference between adjacent A-lines, and Δt_A is the time interval between adjacent A-lines. Doppler angle and blood vessel diameters were determined from the 3D vasculature maps. Absolute blood flow velocity was then calculated from the obtained axial velocity component after being corrected by the Doppler angle of the vessel. We then calculated blood flow rate for each vessel by multiplying the absolute velocity with the area of the vessel cross-section. In order to better assess the effect of IOP on RBF, the flow rates at each level of IOP were normalized and expressed as a percentage of the baseline reading (10 mmHg). In this manner, to evaluate the effect of acute changes in IOP on RBF, we calculated blood flow changes of 15 arteries/veins from a total of 6 animals.

Five eyes provided images adequate to allow us to visualize the peripapillary choroid. Using pixel density as a measure of perfusion, we quantitated changes in peripapillary choroidal perfusion with increasing IOP by measuring the area of choroidal filling at different IOP levels and calculated this as a percentage of area of choroidal filling at baseline (10 mmHg).

For ONH blood flow quantification, since most blood vessels within ONH are capillaries, we were unable to calculate flow in individual blood vessels, as done for RBF. Because OMAG is sensitive to moving particles only, and can separate the blood flow signal from surrounding static tissue, we were able to delineate the flow map using the blood flow signal only. Hence, we elected to quantify ONH perfusion by calculating blood flow volume as a percentage of ONH volume as follows. The ONH shape, to an approximate depth of 150 μm posterior to the choroidal opening, was first segmented from the anterior view 3-D vasculature map using Amira 3D software (Visage Imaging, Inc.). We then set a threshold to obtain a binary 3D flow map where 1 represents area with flow and 0 represents area with no flow. ONH perfusion was then quantified as the percentage of the voxel numbers showing flow signal divided by the total voxel numbers of the segmented ONH volume. More description of this process is presented in the results section, together with images.

The analysis of the microstructures and blood perfusion from each animal were performed on the same 3D OMAG scan. However, for the retinal blood flow measurement, we needed to take extra scans for Doppler analysis to measure the RBF flow velocity. The switch between the 3D scan and Doppler flow measurement scan was automatically controlled by our controlling software, with a time interval less than 1 second.

3. Results

3.1. ONH, retina and choroidal anatomy viewed by OCT/OMAG

OCT/OMAG is capable of producing 3D images of the structure and vasculature of posterior rat eye. The cross-sectional OCT structural image (Fig. 1A) shows a typical anatomy of the rat eye with labeled layers and optic nerve head (ONH) area. The different layers we identified from the image are the nerve fiber layer (NFL), inner plexiform layer (IPL), inner nuclear layer (INL), outer plexiform layer (OPL), outer nuclear layer (ONL), inner/outer segment (IS/OS), retinal pigment epithelium (RPE), choroid (CH) and sclera (SC). Here, the 1300 nm wavelength light source provides an increased penetration depth, as demonstrated by visualization of the sclera and extraocular muscles. Combining this structural image with the

reconstructed 3D image (Fig. 1B) we are able to identify some additional important features of the anatomy, such as the central retinal artery (CRA) and posterior ciliary artery (PCA), arrows in Fig. 1A. Viewed posteriorly (Fig. 1C), a typical UHS-OMAG image focused approximately 150μm posterior to the opening of the choroicapillaris demonstrates that the rat CRA enters the globe inferior to the ONH, which has a horizontally oval or kidney bean shape. Here, the CRA appears lucent in the UHS-OMAG image because blood is moving axial to the OMAG unit, making the flow too fast to be detected by the system, and leading to signal washout. The maximal-intensity projection maps can be viewed anteriorly to see the retinal and choroidal microvasculature (Fig. 1D). A reduced view of the retinal vessels (Fig. 1E) illustrates their relationship to the choroidal opening at the ONH. The choroid and choriocapillaris consist of a dense capillary bed and appears homogeneous, except for the choroidal opening (Fig. 1F). A detailed retinal capillary vessel network can be seen clearly from the retinal microvasculature map alone (Fig. 1G).
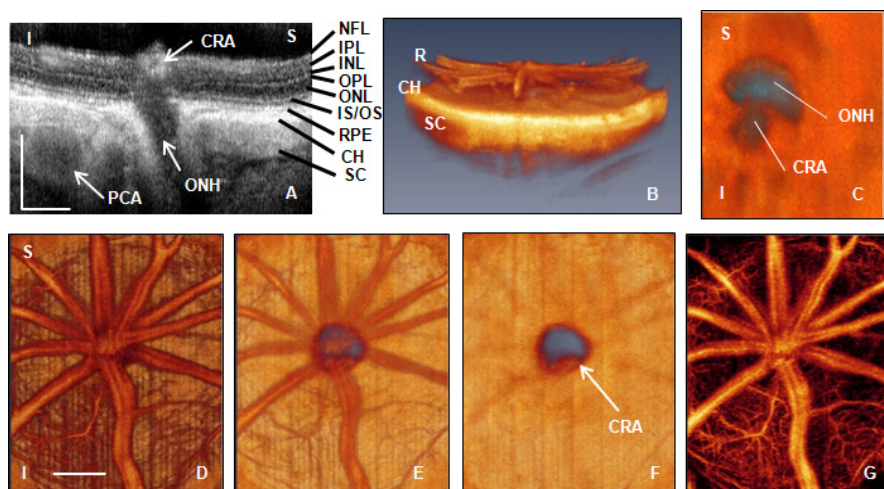

Fig. 1. (A) Cross-sectional OCT structural image showing the layers and ONH anatomy of rat eye. See text for abbreviation definitions. (B) 3-dimensional rendering of OMAG images, showing the microvasculature of the retina (R), choroid (CH) and sclera (SC). (C) Posterior view of UHS-OMAG image approximately 150μm posterior to the opening of the choroicapillaris, showing that the rat central retinal artery (CRA) enters the globe inferior to the ONH. (D–G) Maximal projection maps of the 3-D microvasculature viewed anteriorly as: (D) a combined projection of the retinal and choroidal microvasculature; (E) a reduced view of the retinal vessels to illustrate their relationship to the choroidal opening at the ONH; (F) the choroid and choroicapillaris after removal of retinal vessels, with arrow pointing to the CRA in the inferior aspect of the opening; and (G) retinal microvasculature alone. White bar = 250 μm.

3.2. Effect of elevated IOP on ONH contour

By continuously capturing data at the same longitudinal section, we were able to evaluate the ONH contour change from the OCT structure images at different IOPs (Fig. 2). Here, we termed contour change as a change in the observed surface curvature, compressed retinal and choroidal layers and a distortion of the CRA. When the IOP was lower than 50 mmHg, no apparent contour change was observed. However, IOPs above 60 mmHg progressively compressed the adjacent retina (R) and choroid (CH) and distorted the CRA posteriorly, along with apparent compaction of the ONH. All of these effects resolved completely when IOP was returned to baseline. Horizontally oriented views (Fig. 3) at progressively higher IOPs clearly showed posterior bowing of the retina and choroid around the ONH and posterior displacement of the central retinal vessels (*) into the ONH. Dashed yellow lines were drawn in each panel to serve as a reference (top line: original RPE layer surface; bottom line: 200 microns posterior to the top line). At 80 mmHg we observed an approximately 60 μm

displacement, as denoted by the white arrow point from the original RPE layer surface to the new location (around ONH only).
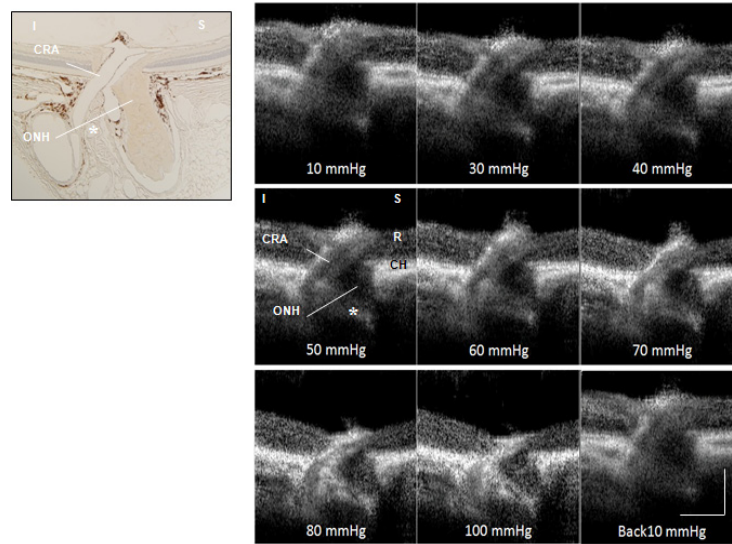

Fig. 2. Compared to a histologic section (Left), vertical longitudinal OCT structure image views of the ONH (right) demonstrate that the central retinal artery (CRA) is located inferior to the optic nerve head (ONH), and separated from it by a band of sclera (*). (Right) Sequential images show posterior displacement of the retina (R) and choroid (C) and compression of the CRA with ONH contour change at increasingly higher IOPs. I = inferior; S = superior. White bar = 200 μm.
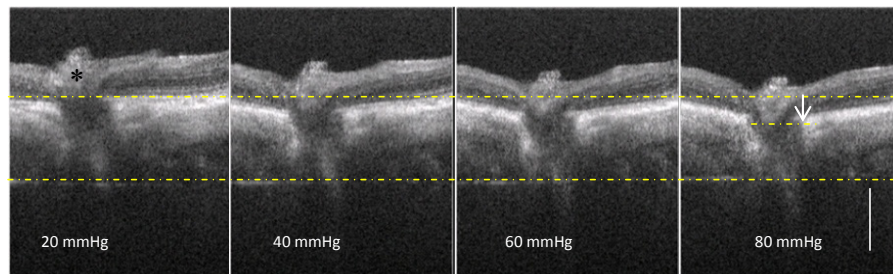

Fig. 3. Horizontal views at higher IOPs show posterior bowing of the retina and choroid around the ONH and the posterior displacement of the central retinal vessels (*) into the ONH with the dashed lines as reference. White bar = 200 μm.

3.3. Effect of elevated IOP on retinal and choroidal perfusion

UHS-OMAG microangiogram maps (Fig. 4A) of the rat RBF showed a progressive decrease in the density of functional capillaries and a decreased diameter of the larger vessels as the IOP was increased from 10 mmHg to 80 mmHg, with near complete obstruction at 100 mmHg. Notably, beginning at 60 mmHg, vertical striping (arrow, Fig. 4) was observed in the UHS-OMAG microangiogram maps, which may be due to increased pulsatility at higher IOPs from reduced ocular perfusion pressure. Apart from visualizing the reduction of RBF, we quantitated the effect of elevated IOP on RBF (Fig. 4B). Average blood flow rate changes from 6 eyes (15 vessels) demonstrated an approximately linear decrease in RBF relative to baseline, starting from 30 mmHg to nearly 0 at 100 mmHg. RBF maps and flow values reverted to baseline after IOP was returned to 10 mmHg. The corresponding vessel diameter changes are given in Fig. 4C, to help identify the contribution of velocity and vessel diameter

to the reduced blood flow rate. This shows that the reduction in vessel diameter was smaller than that of blood flow rate, suggesting that the blood flow rate reduction resulted from decreased flow velocity as well as reduction in vessel diameter. The relatively larger error bars in diameter change are caused by the inherent size difference between veins and arteries and a likely greater effect of increased IOP on the former as opposed to the latter. For interested readers, in the supplementary material associated with this paper, we provided the detailed data sets in absolute units that were used to construct Figs. 4B and 4C. These data sets include the separated results from the arteries and veins, absolute values for vessel diameters (μm), flow velocity (mm/s), and flow rate (μl/min).

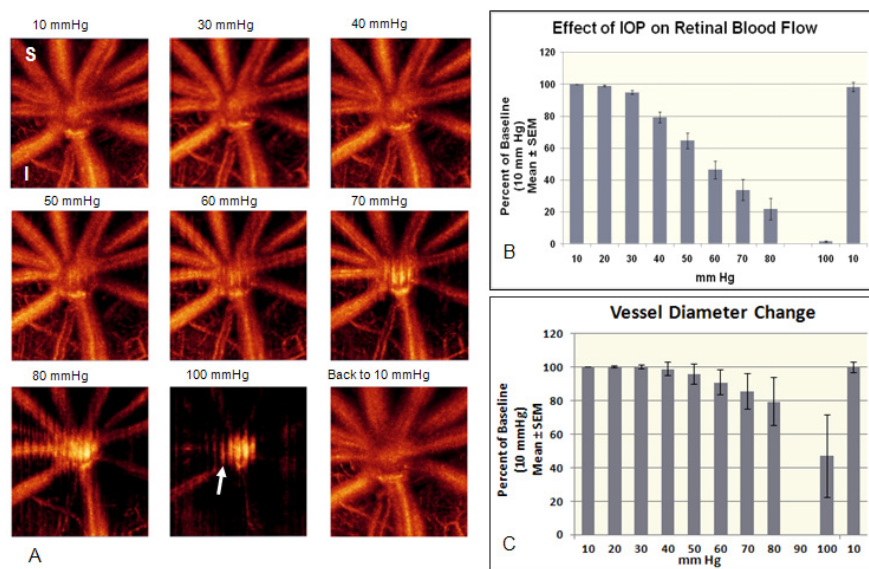
Fig. 4. (A) UHS-OMAG microangiogram maps of the rat RBF at different IOPs. (B) Quantitative RBF data (Mean ± SEM) from 6 eyes (15 vessels) show the relative change of RBF under increased IOPs. (C) The corresponding vessel diameter change. The values in B and C are normalized to the percentage of baseline value (10mmHg).

The appearance of choroidal capillary beds (Fig. 5) at increasing IOP was viewed after removal of the retinal vessels in the post-processing of the 3D OMAG data set. This revealed, at low IOPs, a dense and intact choroidal capillary bed and choroicapillaris with an opening for the ONH. As the IOP was increased, these beds began to show the effects by 60 mmHg, as demonstrated by apparent filling voids (*). Above this IOP, choroidal capillaries were increasingly dramatically compressed, allowing larger choroidal vessels to be visible. At 100 mmHg, even large choroidal vessels appeared closed. Within the ONH, some capillary flow signals (arrows, see also Fig. 7D) were visible up to 70 mmHg, but not above this. As with the RBF, all changes reverted to baseline once IOP was returned to 10 mmHg.

To quantitate the reduced choroidal perfusion or filling with increasing IOP, we measured the area of choroidal filling at each IOP level and calculated this as a percentage of the choroidal filling seen at baseline (10 mmHg) over the whole image size according to the pixel characteristics for 5 eyes (Fig. 6). This showed that, from 10 to 50 mmHg, filling was equal to baseline, which we interpret as no reduction of choroidal perfusion. At 60 mmHg, filling was reduced by 6.5% indicating early effects on choroidal perfusion. Above 60 mmHg, this effect was increased, and at 100 mmHg perfusion was reduced to only 20% of baseline. Again, peripapillary choroidal perfusion returned to normal once IOP was lowered to baseline.
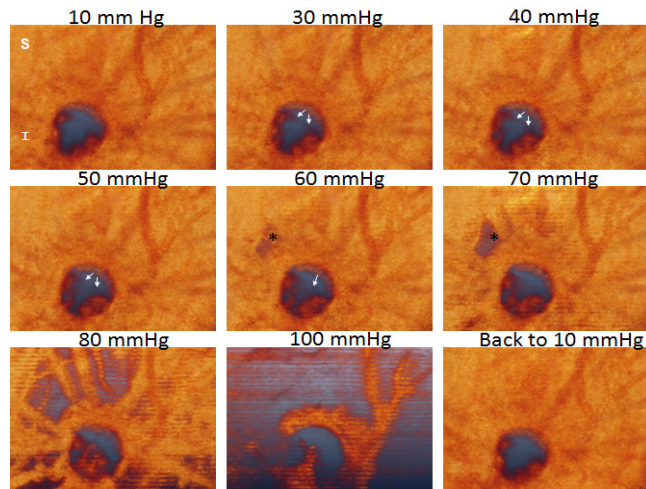
Fig. 5. UHS-OMAG microangiogram of choroidal and ONH capillary beds at increasing IOP from 10 mmHg to 100 mmHg and back to 10 mmHg, viewed after removal of the retinal vessels. Arrows indicate ONH capillary flow signals (also see Fig. 7D), visible up to 70 mmHg. Asterisks indicate appearance of filling voids with increasing IOP.
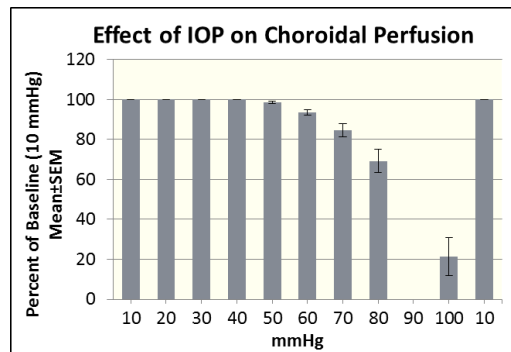

Fig. 6. Quantitative measurement of the IOP effect on the choroidal perfusion illustrated by the percent of perfused choroidal area compared to baseline value at 10 mmHg (Mean ± SEM, n = 5).

3.4. Effect of elevated IOP on ONH blood perfusion

Figure 7 shows the quantitative evaluation of ONH blood perfusion response to increased IOP. Figure 7 (top row) shows typical cross-sectional structure images (A, C) and their corresponding flow images (B, D) across the ONH region at two IOP levels (20 mmHg and 60 mmHg, respectively). The capillary flow signals within ONH can be visualized in Fig. 7D (arrows), however, overlying retinal vessels may shadow the structures within the ONH which results in low signal strength in the OCT image (dashed circle in Fig. 7A), causing some capillary perfusion to be undetectable (Fig. 7B). Figure 7 (middle) shows the steps in quantitation of ONH blood perfusion. These include segmentation of the retinal vasculature from anterior view 3-D vasculature maps (E to F), and then identifying the blood flow signal pixel map (G) and the ONH volume used for the percentage of perfusion calculation (H). After we obtained the binary blood flow pixel maps, the whole segmented binary map, which represents ONH volume, was integrated, the value of which was considered to be the percentage of blood perfusion volume compared to the whole ONH volume. The volume for this data analysis has an approximate depth of 150 μm posterior to the choroidal opening as shown in Fig. 7C. In order to show the effect of acutely increased IOP on the ONH blood

perfusion, we calculated blood perfusion in this manner at each IOP level. A graph of these ONH blood perfusion calculations at increasing IOPs is shown in Fig. 7. This shows an apparent increase in perfusion at lower IOPs, in contrast to RBF (Fig. 4), which decreased. We feel that this is most likely due to the reduced detection of ONH capillary signal by "shadowing" from overlying retinal vessels at the low IOPs (Fig. 7B). As blood flow in the retinal vessels is decreased with higher IOPs, this effect is reduced and the signal improves, until it is diminished by actual reduction in ONH blood perfusion. Above 60 mmHg, this produces a clear reduction that progresses to nearly 0 at 100 mmHg. Again, ONH perfusion reverted to baseline when IOP returned to 10 mmHg.
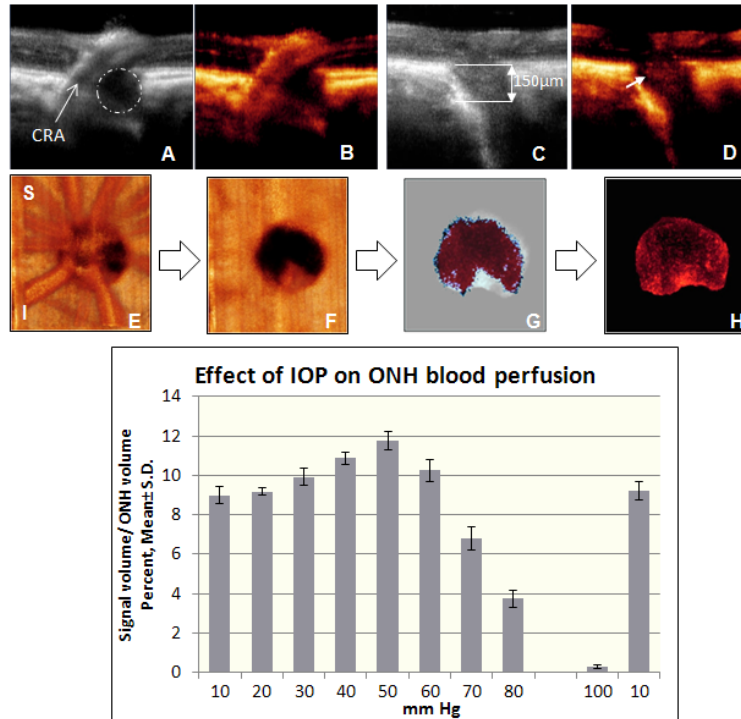

Fig. 7. Top: (A) Typical cross-section OCT structure image (at 20 mmHg) across the CRA where the dashed circle shows the shadowed region, and (B) corresponding flow image of (A). (C) Typical cross-section OCT structure (at 60 mmHg) showing the dimension (between the two lines) for ONH perfusion analysis, and (D) corresponding flow image of (C). Middle: Steps in quantitation of ONH blood perfusion, including removal of retinal vasculature from anterior view 3-D vasculature maps (E to F), generating the blood flow signal pixel map (G) and the ONH volume (H). Image size: 0.5x0.5 mm². Bottom: Graph of ONH blood perfusion (Mean ± SEM) change of 5 animals at increasing IOPs. Up to 50 mmHg, blood perfusion appears to increase, possibly as a result of improved signal detection due to a gradual decrease in the shadowing effect as blood flow in overlying retinal vessels is reduced. Above 50 mmHg, reduction in ONH blood perfusion overcomes this effect and becomes clearly evident, reducing to near 0 at 100 mmHg and returning to baseline when IOP is lowered to 10 mmHg.

4. Discussion

Elevation of IOP is well known to affect retinal perfusion [36], and many investigators maintain that altered blood flow to the ONH may play a role in the development of optic nerve damage in some glaucoma patients, particularly those lacking clear evidence of elevated IOP [37]. In addition, nearly all animal models developed to study the mechanisms of glaucomatous optic nerve damage involve elevation of IOP [29]. However, unless perfusion of the back of the eye can be determined in these models, it is difficult to be certain what role reduced perfusion or ischemia might play in the effects of elevated IOP on the relevant

tissues. For these reasons, developing non-invasive methods of imaging and measuring blood flow in the retina, choroid and ONH is important for both clinical management and experimental research in glaucoma.

OCT/OMAG has now been successfully used to image in vivo microvascular beds, to the capillary level, in several different tissues, including human skin and retinal and choroidal vessels, and in several experimental situations, such as the response of brain and rat skeletal muscle vascular beds to physiologic stimuli [38,39]. Most recently, we have described its adaptation for imaging and measuring blood flow in the retinal vasculature of the rat eye. In this report, we expand on these observations of the peripapillary retina and extend them to the ONH and adjacent choroid. With this, we are provided insights into the unique anatomy of the microvasculature of these structures in the rat eye and demonstrate that this method may be a useful tool to supply quantitative assessment of the response of blood flow to acute elevations in IOP in these different regions.

A significant feature of this system is the use of 1300 nm wavelength light, which allows deeper penetration of ocular tissues than instruments using 800 nm light. The advantage of the deeper penetration is evident from the detailed tissue images of the ONH that even include posterior ciliary vessels, many features of which can be directly correlated with those of a histologic tissue section, as shown in Fig. 2. Of particular importance, 3D maximal projection maps of the peripapillary retina, choroid and ONH (Fig. 1) even include the ONH capillary bed to a depth of 150 µm, a region that is thought to be the site of initial axonal injury in our chronic rat glaucoma model [31,40]. Another advantage of the increased penetration of this system is that it allows us to visualize conformational tissue responses to elevated IOP within the ONH (Fig. 2 and Fig. 3). Fortune and colleagues, using spectral domain OCT with the Spectralis HRA-OCT (Heidelberg Engineering GmbH, Heidelberg, Germany) have recently reported detailed measurements of rat retinal and ONH response to acute IOP elevations of 50 and 70 mmHg [41]. They noted the elliptical choroidal opening that bordered the ONH, and found significant posterior movement of the ONH surface and decreased retinal thickness within this ellipse during elevated IOP. Figure 2 of the current study qualitatively shows posterior movement of the ONH surface at higher IOP, but also demonstrates posterior movement and compression of the central retinal artery, as well as apparent density of the optic nerve itself within the ONH. Quantification of these internal ONH changes is beyond the scope of the current report, but these images suggest the possibility of using this technique to monitor and better understand the physical consequences of cellular responses to elevated IOP, particularly at the site of initial injury, that we have observed in our chronic model of elevated IOP [31,42]. The microvasculature images provide striking in vivo corroboration of prior findings of basic anatomic features of the ONH in the rat that, until now, were only apparent using static ex vivo, histologic methods [43–45]. These features include a consistent presence of the central retinal artery inferior to the horizontally-oriented kidney bean-shaped neural optic nerve at the level of the sclera.

In addition to these anatomic relationships, OMAG/OCT also provides a dynamic view of the ocular vasculature, as shown by our ability to measure microvascular responses to acutely elevated IOP in all three tissue beds. While relatively few studies have been published on the rat microvascular response to elevated IOP, our results (Fig. 4) are in general agreement with those of He and colleagues [9] who, using the laser Doppler flowmetry, noted that an IOP of 50 mmHg was associated with a reduction in ocular blood flow to approximately 50% of baseline, as compared to our finding that a similar IOP level produced a less severe reduction in flow, to just over 60% of baseline. At higher IOP, we observed vertical striping of the vessels in the UHS-OMAG microangiogram maps, which we interpreted as increased pulsatility of the vasculature as perfusion pressure nears diastolic pressure. Because ocular perfusion is dependent on systemic blood pressure, we also measured the effect of 2% isoflurane via the femoral artery in a separate group of similar-aged rats, revealing a mean systemic blood pressure (± SEM) of 106 ± 4 mmHg (N = 5). This is comparable to published experience with isoflurane as well as other anesthetics [9,46–49] and is consistent with the

increased pulsatility observed by OMAG/OCT. Similarly, Fortune and colleagues noted significant attenuation of the retinal vessels when IOP was raised to 70 mmHg [41].

Interestingly, Bui and colleagues [9] observed an almost immediate reduction in blood flow with elevated IOP, while, with OMAG/OCT, we found that, while RBF did show an initial decrease below 30, this accelerated to a linear reduction above 30 mmHg. This may suggest evidence of autoregulatory mechanisms that may be overcome once perfusion pressure is reduced to a critical level. This phenomenon, which appears to be operative up to an IOP of 30 to 40 mmHg, has been extensively studied in the retina and ONH in humans [4,50,51] and in non-human primates [36] as well as other animals [52,53]. Images of the choroidal microvasculature are dominated by the capillary beds of the choroid and choriocapillaris that are too small and dense to discriminate, which results in a generalized, uniform signal. Because of this, blood flow velocity in individual vessels cannot be determined, as done for the retinal vasculature. However, we were able to quantitate percent choroidal filling by measuring areas of non-perfusion at increasingly higher IOPs. Using this, we noted that choroidal "perfusion" remained stable over a surprisingly wide range of IOPs, and only began to deteriorate noticeably at 60 mmHg, with a rapid drop above this level (Fig. 6). While choroidal perfusion has classically been considered to be influenced solely by ocular perfusion pressure [54], other work in animals and humans suggests that choroidal autoregulation may occur [55,56]. While it is tempting to interpret our current data as further evidence of choroidal autoregulation, this is only a measure of choroidal filling, and not strictly a measure of choroidal flow, as the flow rate within the capillary beds still being perfused is unknown. Further refinements, perhaps using measures of pixel density within these beds may improve our ability to use OMAG/OCT for a more accurate assessment of choroidal perfusion.

Perhaps the greatest potential for the use of OMAG/OCT for assessing mechanisms of glaucomatous injury in the rat eye is its ability to measure ONH blood perfusion. While this did reveal a reversible reduction in perfusion at higher IOPs, we encountered a shadowing and tailing effect caused by overlying major retinal vessels. As mentioned above, this will affect the observed blood perfusion signal within the ONH, especially when the large retinal vessels are fully perfused at lower IOP levels. This likely results in a false increase in measured blood perfusion within the ONH as the IOP increases from 10 mmHg to 50 mmHg, and retinal flow is reduced. In order to solve this problem, one possible approach could be to use measured RBF change to compensate for the impact of this shadowing effect on measured ONH blood perfusion. The study of the relationship between measured ONH perfusion and the overlying RBF is currently ongoing.

5. Conclusion

In conclusion, we have used an OCT/OMAG system to image the posterior eye of the rat. Using a wavelength of 1300 nm for increased penetration, we were able to image the structural and vascular anatomy of nearly the entire thickness of the ONH, and the adjacent choroid and retina, and demonstrate the effects of acutely elevated IOP on these structures. Quantitative measurements of the effect of elevated IOP on the RBF, and choroidal and ONH perfusion as determined by this technique are presented as well. Starting from 30 mm Hg, the RBF diminished linearly with increasing IOP and was nearly extinguished at 100 mm Hg. Choroidal perfusion did not appear to be affected until 60 mmHg, above which further reductions developed exponentially. Both of these effects fully recovered after IOP was returned to baseline. A reduction in ONH capillary blood perfusion at higher IOP's was also observed, but shadowing and tailing from perfusion of overlying retinal vessels at lower IOP's limited precise measurements of change compared to baseline ONH perfusion. This technique may prove useful in evaluating the contribution of altered retinal, choroidal and ONH perfusion to optic nerve and retinal damage in rodent glaucoma models that employ elevated IOP.

Acknowledgments